Photoacoustics 36 (2024) 100589

Contents lists available at ScienceDirect

Photoacoustics

journal homepage: www.elsevier.com/locate/pacs

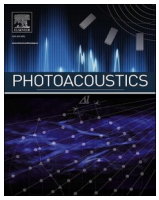

Non-invasive evaluation of endometrial microvessels via in vivo intrauterine photoacoustic endoscopy

Qingrong Xia [a,b,c,d,1], Shengmiao Lv [c,d,1], Haoxing Xu [c,d], Xiatian Wang [c,d], Zhihua Xie [c,d], Riqiang Lin [c,d,e], Jinke Zhang [c,d], Chengyou Shu [c,d], Zhiyi Chen [a,f,*], Xiaojing Gong [c,d,**]

[a] Institute of Medical Imaging, University of South China, Hengyang 421001, China
[b] Affiliated Nanhua Hospital, University of South China, Hengyang 421002, China
[c] Research Center for Biomedical Optics and Molecular Imaging, Key Laboratory of Biomedical Imaging Science and System, Shenzhen Institute of Advanced Technology, Chinese Academy of Science, Shenzhen 518055, China
[d] Shenzhen Key Laboratory for Molecular Imaging, Guangdong Provincial Key Laboratory of Biomedical Optical Imaging Technology, Shenzhen Institute of Advanced Technology, Chinese Academy of Science, Shenzhen 518055, China
[e] Department of Electrical and Electronic Engineering, The Hong Kong Polytechnic University, Hung Hom, Kowloon, Hong Kong, China
[f] Institution of Medical Imaging, The Affiliated Changsha Central Hospital, Hengyang Medical School, University of South China, Changsha 410000, China

ARTICLE INFO

Keywords:
Intrauterine photoacoustic endoscopy
Non-invasively
In vivo
Microvessels
Endometrial receptivity
Quantitative evaluation

ABSTRACT

The endometrium microvessel system, responsible for supplying oxygen and nutrients to the embryo, holds significant importance in evaluating endometrial receptivity (ER). Visualizing this system directly can significantly enhance ER evaluation. Currently, clinical methods like Narrow-band hysteroscopy and Color Doppler ultrasound are commonly used for uterine blood vessel examination, but they have limitations in depth or resolution. Endoscopic Photoacoustic Imaging (PAE) has proven effective in visualizing microvessels in the digestive tract, while its adaptation to uterine imaging faces challenges due to the uterus's unique physiological characteristics. This paper for the first time that uses high-resolution PAE in vivo to capture a comprehensive network of endometrial microvessels non-invasively. Followed by continuous observation and quantitative analysis in the endometrial injury model, we further corroborated that PAE detection of endometrial microvessels stands as a valuable indicator for evaluating ER. The PAE system showcases its promising potential for integration into reproductive health assessments.

1. Introduction

The successful implantation of the embryo is a crucial determinant of a successful pregnancy, and it involves a complex interaction between the endometrium and the blastocyst. The ability of the endometrium to support normal embryo implantation is referred to as endometrial receptivity (ER), which forms the foundation of pregnancy [1]. It is estimated that about 2/3 of embryo implantation failures can be attributed to inadequate ER in assisted reproduction [2]. Impaired ER is an important limiting factor in the pursuit of improving clinical pregnancy rates, making it a central area of focus and challenge within reproductive medicine research.

There are several common factors that affect ER, such as endometrial thickness, pattern, blood supply and other factors [3]. Among these, the microvessels located in the intima play a direct role in supplying essential oxygen and nutrients to the embryo, which could significantly influence the success rate of embryo implantation [4,5]. Consequently, evaluating the microvessels holds particular significance in assessing ER [6]. However, the existing methods for clinical evaluation of microvessels are suboptimal. Traditional hysteroscopy, a minimally invasive surgical technique performed in the uterine cavity, has gained extensive usage in diagnosing and treating uterine conditions [7]. Nevertheless, it has poor contrast and specificity in visualizing blood vessels. The Narrow-band imaging (NBI) hysteroscopy technology offers notable

* Corresponding author at: Institute of Medical Imaging, University of South China, Hengyang 421001, China.
** Corresponding author at: Research Center for Biomedical Optics and Molecular Imaging, Key Laboratory of Biomedical Imaging Science and System, Shenzhen Institute of Advanced Technology, Chinese Academy of Science, Shenzhen 518055, China.
E-mail addresses: winchen@vip.163.com (Z. Chen), xj.gong@siat.ac.cn (X. Gong).
[1] These authors contribute equally to this work.

https://doi.org/10.1016/j.pacs.2024.100589
Received 8 September 2023; Received in revised form 9 January 2024; Accepted 17 January 2024
Available online 24 January 2024

advantages, including enhanced visualization of superficial lesions and microvessels architecture during endoscopic procedures [8]. While NBI hysteroscopy is limited to visualizing blood vessels only on the superficial surface of the endometrium without depth resolution. Utilizing color Doppler, transvaginal ultrasound captures endometrial blood flow at various depths, showcasing the vascular arrangement. Power Doppler can enhance the visualization of small blood vessels [9]. However, transvaginal ultrasound only allows for the observation of the uterine cavity at the external of the cervix. The presence of cervical tissue and the extensive imaging distance significantly impede its sensitivity and resolution in practical applications, thereby posing challenges in visualizing the microvessels or microvascular network in the endometrium.

Based on the photoacoustic effect, photoacoustic imaging (PAI) is an emerging non-invasive biomedical imaging technique. PAI utilizing endogenous optical absorption contrast has enabled in vivo vascular imaging with capillary-level spatial resolution [10], making it a prominent tool with three-dimensional (3D) views for examining morphological changes in the vascular network [11]. Photoacoustic endoscopy (PAE), which incorporates PAI into a miniaturized probe, presents a novel and minimally invasive diagnostic tool capable of delivering optical spatial resolution and optical absorption-based contrast [12]. PAE enables high-resolution imaging of the microvascular network within the lumen in an in vivo setting. Within the gastrointestinal tract domain, gastrointestinal PAE allows for the visualization of blood vessel distribution in the gastrointestinal tract wall, aiding in the detection of tumors [13]. According to the report, Prof. Christopher Miranda's team have achieved the pioneering application of PAE in vitro within the pig uterus, demonstrating PAE's imaging capability concerning blood within the uterine wall. This signifies the prospective use of PAE in diagnosing endometrial diseases. However, this research primarily focused on in vitro imaging within the uterus, and as far as we know, PAE systems have yet to be reported on endometrial imaging in vivo [14]. The main obstacle is the unique nature of the uterus in small animals, including the uterine cavity is difficult to enter through the vagina and cervical canal, the endometrial vascular network is abundant and intricate, which poses significant challenges to achieving high-resolution microvessel network images in a non-invasive way and presenting another obstacle in feature extraction and quantification analysis.

In this study, we present a novel intrauterine PAE system that enables in vivo imaging within the rat uterine cavity, providing the first-ever presentation of endometrial microvessel non-invasively. Through continuous observation of the rat endometrial injury model, we successfully caught the trends of the endometrial microvessels and quantified the microvessel density (MVD) to evaluate this observation. Subsequent pregnancy experiments have further confirmed that the quantitative results of PAE have a correlation with the success rate of conception. Our work with small animal models demonstrates the promising clinical potential of the in vivo non-invasive evaluating ER.

2. Materials and methods

2.1. Imaging system and miniature catheter

The PAE imaging system closely resembles our previous work [15], incorporating nanosecond pulsed lasers (MIRON-DPSSL-PL-1064 & 532), a coupling optical path, optical-electric slip ring (PT1-Z8,Thorlabs), ultrasound pulser/receiver (5073PR, Olympus, Japan), and with a

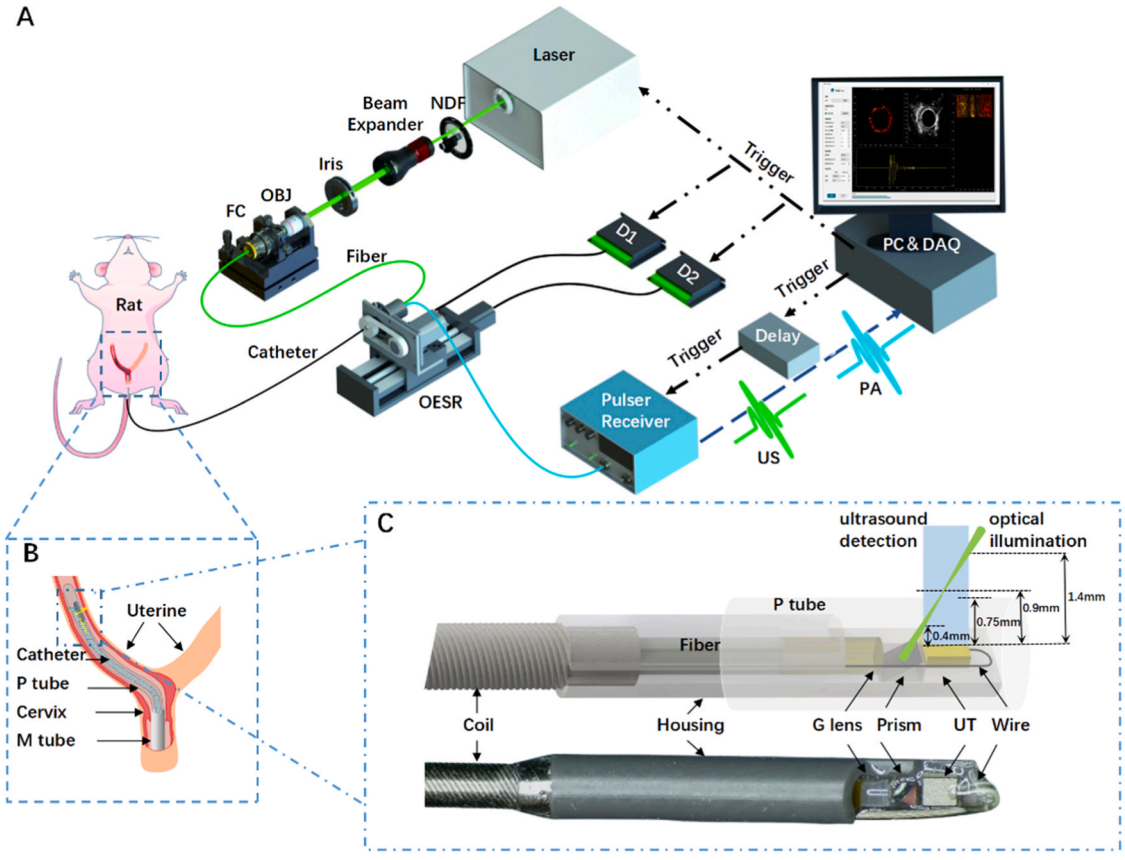

Fig. 1. (A) The diagram of the PAE imaging system in the rat uterine cavity; (B) the non-invasive imaging process of an endoscopic catheter in rats uterine; (C) the overall schematic and photo of the distal end of the PAE catheter, including the overlay between the optical illumination and ultrasound detection. PC & DAQ: personal computer and data acquisition; OBJ: objective; FC: fiber coupler; OESR: optical-electric slip ring; US: ultrasonic; PA: photoacoustic; UT: ultrasound transducer; P tube: protective tube; M tube: metal tube; G lens: GRIN lens.

PC-based data-acquisition system (ATS9325, Alazar Tech, Canada), as illustrated in Fig. 1A. In the research, the laser at the wavelength of 532 nm and laser energy of 1.5 μJ is used for photoacoustic excitation. The OR-PAE catheter was designed as illustrated Fig. 1C. The laser beam emitted from the optical fiber was initially focused using a gradient index lens (64515, Edmund Optics, USA), and then redirected to the endometrial surface by a custom-made 34° prism (Fuzhou OYeah Optronics Co., Ltd, Fujian, China). The focal point of the beam was specifically set at 0.9 mm from the center of the catheter. The overlay between the optical illumination and ultrasound detection is about 1 mm (ranging from 0.4 mm-1.4 mm) as described in Fig. 1C. Positioned behind the prism was a transducer (40 MHz, 40% bandwidth, Blatek, USA) to ensure high resolution and sufficient detection efficiency. The outer diameter of the protective tube used in our experiment is 1.5 mm, and the material is PA12. By measuring the optical energy of the catheter and the signal intensity of the emitted ultrasound with and without the protective tube, it can be known that the optical transmittance of the protective tube is about 93% and the ultrasound transmittance is about 76%. The catheter was completely immersed in the protective tube during imaging, and all experimental data in this work were performed with the protective tube. In addition, the whole catheter is driven through a double-layer coil (Tu's Cheng Fa, China) to perform rotation and pullback movements.

2.2. Imaging procedure

During imaging, the catheter is driven by the slip ring, enabling rotation and pullback. The imaging scanning speed is 6.25 fps (frames per second), with each B-scan comprising 1600 A-Lines. The pullback operates at a step of 10 μm each frame. And the pullback speed in our system is 62.5 μm/s.

To validate the catheter's performance, the imaging resolution is assessed first. A knife-edge is employed to traverse the excitation laser beam emitted by the catheter with a 5-μm step at the focal position. A photodiode, placed behind the knife, records the changes in beam energy as the knife-edge is moved to different positions. Then we can get the horizontal resolution. The axial resolution is measured by the pulse-echo method using a glass block. From the results we can obtained the transducer frequency and echo characterization, based on the equation $R_{Axial} = \frac{0.88 \bullet v_s}{\Delta f}$ [16] we can get the axial resolution.

For animal in vivo imaging, the initial step involves establishing a non-invasive route by a metal tube carefully inserted through the vaginal canal into the uterus as described in Fig. 1B. The front end of the protective tube is generously lubricated and then carefully put the catheter into it. Through the non-invasive path, the assembly is guided into the rat's uterine cavity until it reaches the uterine horn. Once positioned, the photoacoustic imaging procedure, as illustrated in Fig. 1A, is executed.

2.3. Animal models

All Sprague Dawley (SD) rats (female: 9–13 weeks old, weighing 200–300 g; male: 10 weeks old, weighing about 300 g, Guangdong Vital River Laboratory Animal Technology Co. Ltd.) were bred and housed under standard conditions. The experiment rats displayed regular estrous cycles and all experiments were performed under isoflurane anesthesia. All experiments conducted on animals have adhered to the protocols that had been approved by the animal study committee of the Shenzhen Institute of Advanced Technology, Chinese Academy of Sciences (approval number: SIAT-IACUC-220811-YGS-GXJ-A2179).

The experimental rats were categorized into three distinct groups: the normal control group, the mild and the severe injury group, each comprising 3 rats. In the normal control group, put the modeling tool into the uterine cavity without additional procedures. The electric heating catheter was used to model the mild and severe groups at temperatures of 55 °C and 85 °C, respectively, for a duration of 5 s [17]. It is administered via the vaginal route into the uterine cavity non-invasive pathway as depicted in Fig. 1B. Photoacoustic imaging was conducted on both the normal control and model groups on days 0 and 3 after modeling. Each rat underwent a pathological examination for comparison after the photoacoustic imaging.

Each group of 3 rats was paired with a weight-matched male rat. Successful mating was confirmed by the presence of a vaginal plug or sperm was observed under the microscope and the day was marked as embryonic day 1 (E1). At E12-E15 pregnant females were sacrificed and embryos were counted.

2.4. Histopathology procedure

After being imaged, the rats were euthanized, and their uteri were collected, rinsed, and fixed in a 4% paraformaldehyde solution for 12 h before undergoing further processing. The tissue samples were dehydrated using a continuous ethanol solution, embedded in paraffin and sectioned. Stainings of HE and Masson were used to evaluate the structure of the injured uterus at the histological level. CD31 immunohistochemical staining was performed to observe the endometrial microvessel formation in each group. The endometrial morphology was examined using a slide scanner, while microvessels were observed with a fluorescent microscope (Olympus, Japan).

2.5. Image processing

The raw data acquired by the imaging system undergoes denoising through a band-pass filter. Subsequently, the Hilbert transform is employed to extract the signal envelope and construct it into 3D volume data. To enhance the visualization of the 3D imaging results, this paper utilized an algorithm based on transparency (alpha) blending and depth color coding, which is termed Depth blending Alpha Projection (shorted as DAP). Each pixel is encoded in the Alpha, Red, Green and Blue (Alpha-RGB) format. The RGB values represent the depth of the signal, implying that signals at different imaging depth positions are assigned distinct colors. The transparency value is directly proportional to the signal amplitude of the pixel and is normalized within a range of 0 to 1. When the alpha value of a pixel is 0, it indicates complete transparency, allowing signals from deeper positions to be visible. On the other hand, when the alpha value of a pixel is 1, it represents complete opacity, rendering any signal located deeper entirely invisible. By stacking the data along the depth direction using the principle of transparency blending, we can display the 3D data in a two-dimensional (2D) manner. The detailed description of this method can be found in Supplementary Fig. 11. For comparing this with the original 2D data, data from some certain same depth is displayed in the horizontal slice figure manner.

During the quantification process, the initial step involves selecting the data of background area to calculate the standard deviation value of noise, denoted as T_i. Subsequently, the average of all T_i values is calculated and recorded as T, serving as the threshold for blood vessel binary segmentation. To calculate the MVD, each DAP or slice figure is binarized using the threshold T. At each B-scan position of the DAP or the slice images, we calculate the MVD by determining the ratio of pixels with a value of 1 (representing vessels) after binarization to the total number of pixels along the line (representing the corresponding whole B-scan space or specific depth in the B-scan). After this, the MVD versus pullback distance curves extracted respectively from DAP and slice figures are plotted, corresponding to DAP and slice results. In addition, the density distributions are statistically analyzed for each group based on these MVD curves and showcased in histograms. Finally, the characters of density distributions in the modeling areas of each group are compared with the pregnancy results.

3. Results

Fig. 2 shows the results of endometrial microvessels in normal rats with different imaging modalities. From these figures, we can see that the endometrial microvessels are very dense and distributed in a basket-like pattern, the same as the literature reported before [18]. From Fig. 2A, the MicroCT images the distribution of endometrial blood vessels macroscopically, which is performed after the injection of the contrast agent. The microvessels cannot be clearly visualized in the original MicroCT or its local enlarged image. Fig. 2B and C are the photoacoustic images and the complete endometrial microvessles network imaging can be found in the Supplementary video. Photoacoustic DAP has shown 3-D renderings of microvessel structures in the endometrium, compared with 3D DAP image, part of the blood vessel information is missing in the photoacoustic 2D slice image, resulting in a discontinuous vascular network. CD31 staining in the Fig. 2D shows the microvessels of the top surface layer of endometrium. It can be only seen that the endometrial microvessels are very rich, but the morphological and structural characteristics of the microvessels cannot be visualized. Fig. 2E-G presents sequentially normal rat endometrium B-scan images of endoscopic ultrasound, photoacoustic, and merged results. As can be seen from the zoomed views of Fig. 2F, the depth-resolved microvessels pattern is visible in the picture. The Supplementary Fig. 2 illustrates that the most profound signal originates from a depth of approximately 1.22 mm. This demonstrates that the penetration depth of this system is at least 470 μm.

Fig. 3 displays the photoacoustic DAP images alongside the corresponding CD31 staining images, illustrating alterations in endometrial microvessels across different levels of damage on both day 0 (labeled as M0, S0 for mild and severe injury respectively) and day 3 (labeled as M3, S3 correspondingly). Upon imaging on day 0, mild endometrial injury exhibited a weak residual photoacoustic signal within the modeled area (labeled as the yellow box) no matter in DAP or slice images, and in cases of severe injury, the modeling area (labeled as the yellow box) displayed an even less discernible photoacoustic signal in the modeling area. Some segments within the modeling area vicinity demonstrated a enhanced photoacoustic signal, marked by the white arrow, often associated with bleeding. By day 3, there was a noticeable increase in the photoacoustic signal within the modeling area of mild injury, while remained relatively unchanged for severe injury. These aforementioned changes in photoacoustic images align with the alternations observed in CD31 staining. Fig. 3 displays the results from one sample in each group, the rest can be found in Supplementary Fig. 3 and Fig. 4.

Fig. 4 presents the results of MVD extraction results along the circumferential direction from photoacoustic DAP and slice images, contrasting normal and damaged endometrial conditions. Notably, the MVD observed in the photoacoustic DAP images surpasses that seen in the slice images. All of the MVD results of the normal group were distributed within a relatively narrow range (as shown in subfigures labeled with C) and its value exceeded that of the whole model group, no matter in DAP or slice. In both mildly and severely damaged areas (as marked by the yellow box in subfigures labeled with M0 and S0), a substantial drop in MVD is evident. Notwithstanding, in the mildly damaged areas, an evident resurgence in MVD occurs after a span of three days, while the increase in severe injury is less clear (as marked by the yellow box in subfigures labeled with M3 and S3). Fig. 4 displays the results from one sample in each group, the remaining results can be found in the Supplementary Fig. 5. Morphological changes at different degrees of endometrial injury in the endometrium were indicated by HE and Masson staining can be seen in Supplementary Fig. 8.

The histograms in Fig. 5 illustrate the distribution of MVD across all rats in each group. The density distribution of the normal group exhibits a single-peak characteristic. The densities extracted from the photoacoustic DAP images of the normal group predominantly cluster around

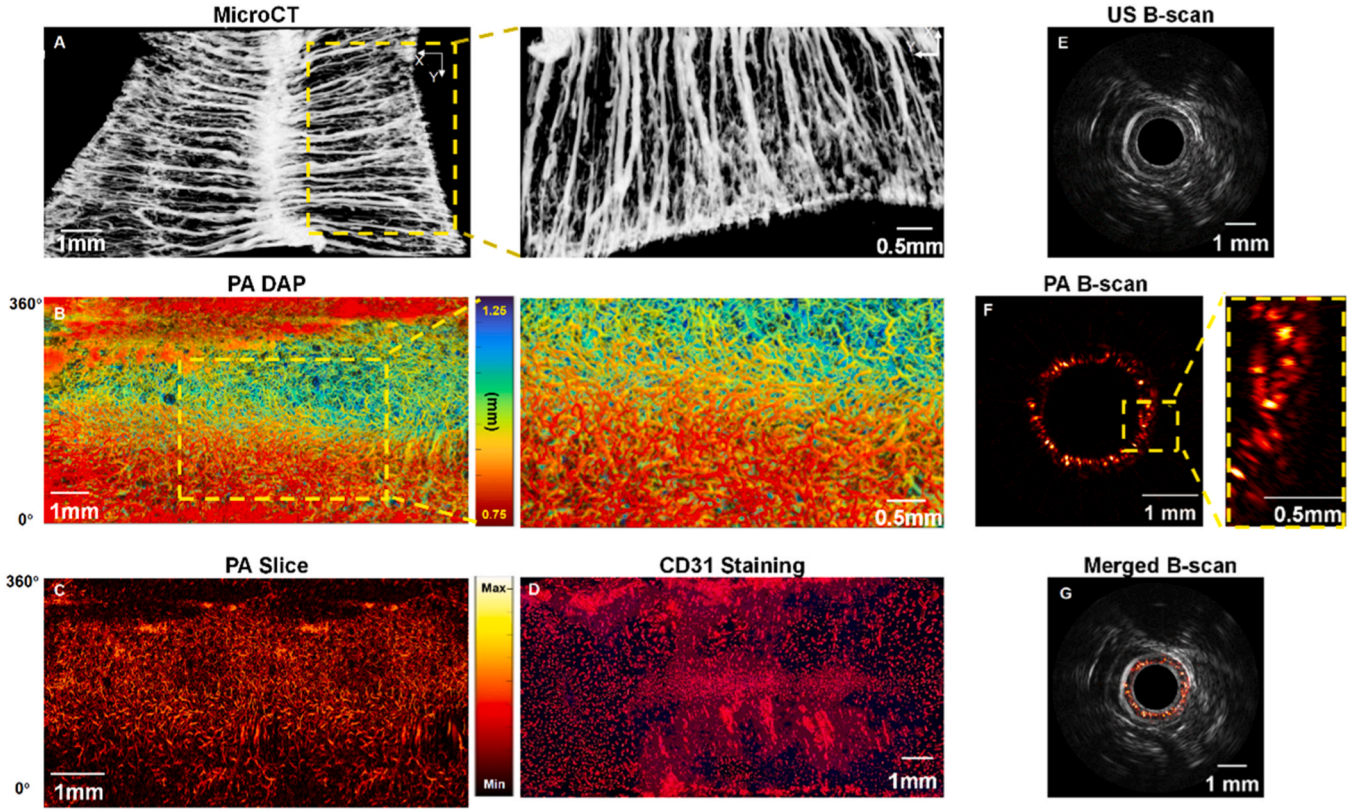

Fig. 2. Microvessels in normal rat endometrium in different imaging modalities. (A) MicroCT imaging result and its local magnification image; (B) photoacoustic DAP result and its local magnification image; (C) photoacoustic slice image at a depth of about 300 μm; (D) the CD31 staining result; (E-G) ultrasonic, photoacoustic B-scans with its local enlarged, and merged B-scan. The yellow box represents the local microvessels. US: ultrasonic; PA: photoacoustic.

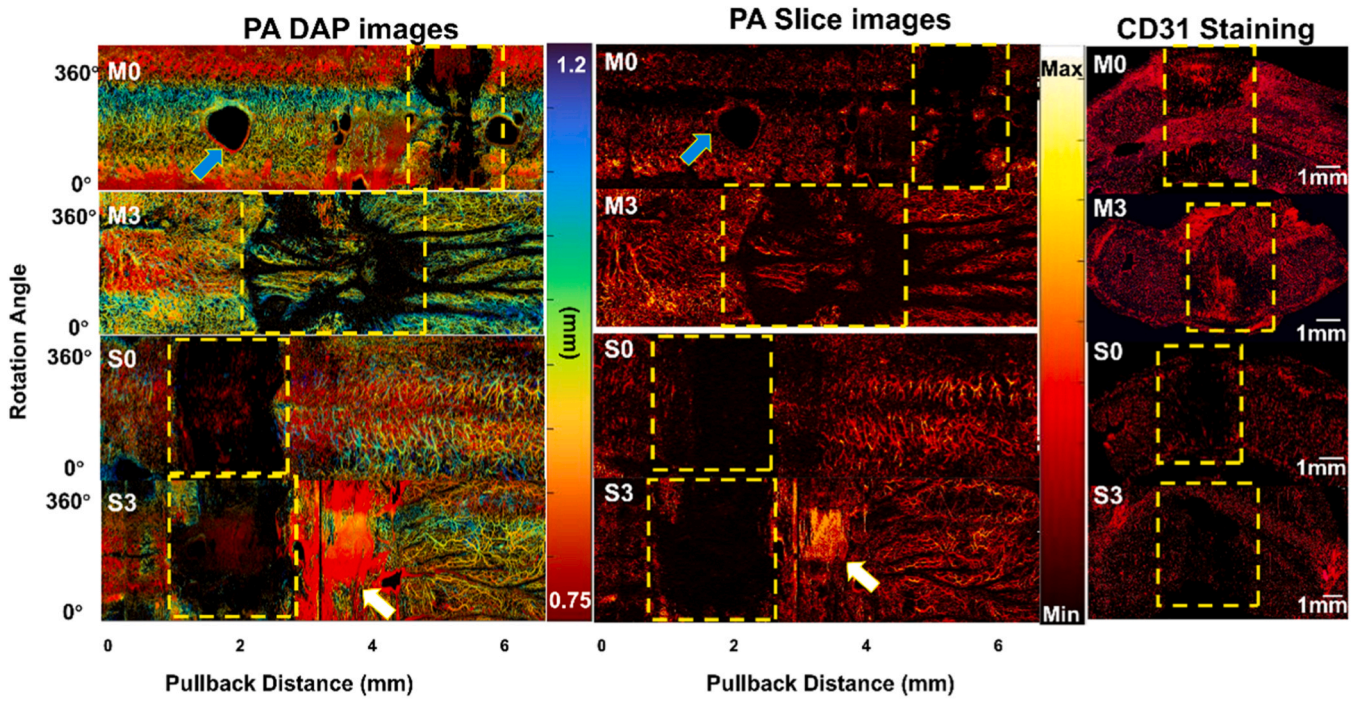

Fig. 3. Images in PA DAP, PA slice and the CD31 staining depict varying degrees of endometrial injury on both day 0 and day 3. M0: on the day of mild injury; M3: the third day after mild injury; S0: on the day of severe injury; S3: the third day after severe injury; the yellow box represents the injury area; the blue arrow represents the air bubble; the white arrow means the hemorrhage.

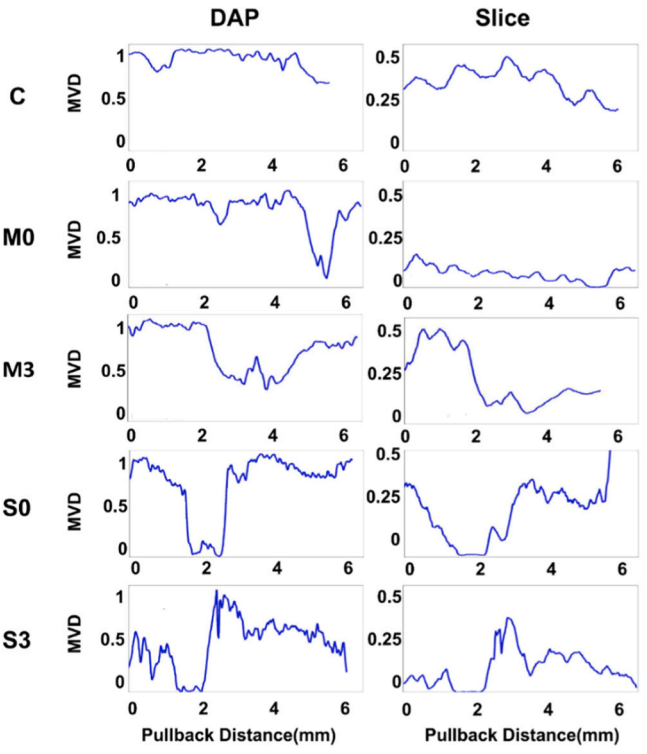

Fig. 4. The results of MVD extracted from photoacoustic DAP and slice images in Fig. 3 respectively. C: the normal one; M0, M3, S0 and S3: the same as labeled in Fig. 3.

0.9, and the slice images tend to center around 0.4, as shown in subfigures labeled with C. The density distribution of the damaged group displays a bimodal characteristic in DAP results. One peak corresponds to the normal area, characterized by relatively high density, and the other peak represents the damaged area with notably lower density, as shown in subfigures labeled with M0 and S0. The severe groups exhibit considerably higher peaks at low density, compared with the mild group. For the results of day 3, as shown in subfigures labeled with M3 and S3, a noteworthy shift is evident in the mild group, transitioning from a bimodal structure to a single-peak pattern. Meanwhile, the severe group microvessels density distribution is essentially unchanged. All slice results have a corresponding similar characteristic but are not clear enough. Notably, a common divide valley separating the normal and damage peaks can be observed in each group of DAP results, with a central value of approximately 0.66, labeled in red dotted lines as shown in Fig. 5. Thus, the value is applied to determine the modeling area in furthermore analysis.

For each group of three rats, the summarized quantification results of endometrial MVD of both the damaged area (highlighted within the yellow box in the photoacoustic DAP image in Fig. 3) and the fertility results are listed in Table 1. In the results corresponding to day 0, the MVD within the mildly damaged area plummeted to 0.25, and the severely damaged area experienced a more pronounced decline to 0.14. Advancing to the results of day 3, the MVD within the mildly damaged area rebounded to 0.56, whereas the severely damaged area's recovery was comparatively modest, reaching 0.34. Meanwhile, the fertility experiment also verified the results.

In the normal group, the total number of embryos on the modeling tool inserted side was 20, and the blank control on the opposite side (the left side) received 24 embryos. The mild injury group displayed a total of 20 embryos on the modeling side (the right side) and 22 embryos on the opposing side. The severe injury group exhibited a single uterine embryo on the modeling side and 19 embryos on the contralateral side. For further insights, kindly refer to Supplementary Fig. 9, which presents the histogram of the average number of embryos in the bilateral uterine cavity of different groups, and the representative photos of embryos from each group.

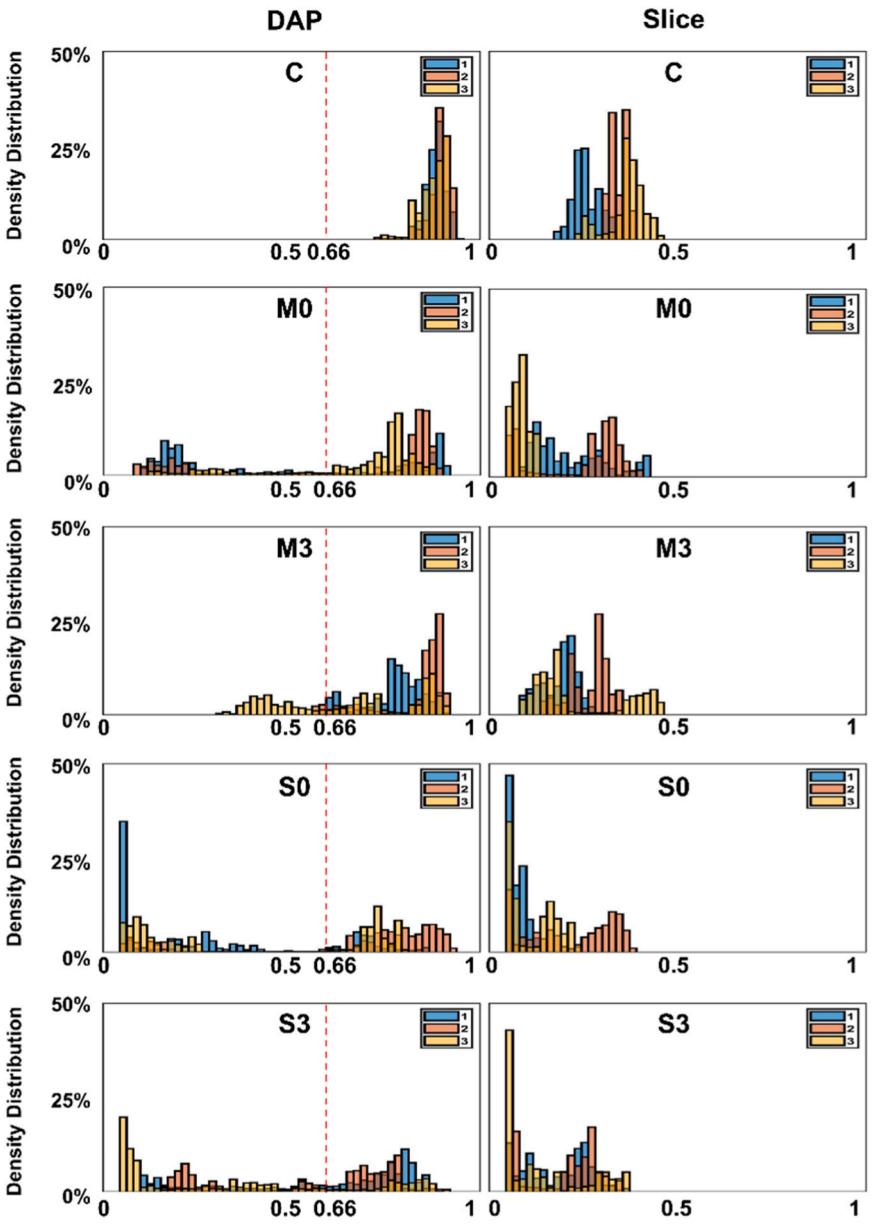

Fig. 5. Density distribution of each group as Fig. 4(N = 15, n = 3 for each group) was combined and graphed. Different colors stand for different individuals. The red dotted line represents MVD= 0.66; C, M0, M3, S0 and S3: the same as labeled before.

4. Discussion

Sufficient endometrial blood flow and perfusion are essential, as they prime the endometrium for the implantation process and significantly influence ER [19]. In the context of successful embryo implantation, the assessment of local microvessels in the endometrium holds great importance [20]. In this study, we have achieved a significant breakthrough by successfully establishing a non-invasive access route within the uterine cavity of in-vivo rats, redesigning a PAE catheter specifically tailored for the rat uterus, and implementing advanced image processing techniques to enable continuous observation of endometrial microvessels.

PAE has been previously reported to characterize the digestive tract vascular network in small animals [13,14,18,21]. While, the dimensions and endometrial thickness of the uterine cavity exhibit significant differences compared to the digestive tract, with the endometrial blood vessels being notably more abundant and densely distributed. To meet the requirements of microvessels photoacoustic imaging in the endometrial region, we performed an optical design specifically tailored to the depth range and distinguishing microvessels within the endometrial layer (~400 μm), which is consistent with the endometrial thickness of rats measured under the support of a protective tube in our preliminary experiment (Supplementary Fig. 10). The results depicted in Supplementary Fig. 1 provide evidence that the newly developed PAE system successfully achieves an adequate depth range (0.75–1.25 mm) and resolution (lateral resolution 28.1 μm, axial resolution 70.9 μm) for imaging endometrial microvessels and distinguishing closely situated vessels. Incorporating the protecting tube, safeguards the endometrium from potential scratches induced by the catheter, and inflates the uterine cavity to lessen the folds on the endometrium. Finally, we achieved comprehensive imaging of the endometrial microvessel network, thus providing a necessary foundation for the continuous observation and quantitative analysis of endometrial microvessels.

As the challenges we encountered before [22], the unique anatomical location and physiology of the uterus in small animals pose a vulnerability issue during the insertion process compared to endoscopy

Table 1
MVD results from Fig. 5 (N = 15, n = 3 for each group). N.A. represents not applicable. Table 1.2. Statistical fertility results from distinct sides of the uterine cavity across three rats in each group (N = 9, n = 3 for each group). C_R, C_L; M_R,M_L, S_R,S_L: bilateral uteri in three groups, the right side is the modeling side except the C_R (the modeling appliance enters but without doing anything in the normal rat), and the left side is the blank control side.

The average MVD in the modeling area				
Number of group	1	2	3	Mean
Groups				
C	N.A.	N.A.	N.A.	N.A.
M0	0.2307	0.1958	0.3351	0.2538
M3	0.6234	0.608	0.4615	0.5643
S0	0.1472	0.1653	0.1188	0.1437
S3	0.3577	0.3039	0.3499	0.3371

Number of embryos per uterus of the rats in each group				
Number of group	1	2	3	Total
Groups				
C_R	8	9	7	24
C_L	8	7	5	20
M_R	6	7	7	20
M_L	7	7	8	22
S_R	0	0	1	1
S_L	5	9	5	19

in the gastrointestinal tract, where direct catheterization is feasible. However, in our study, we successfully achieved a non-invasive insertion by building a channel through the vagina into the uterine cavity. Such non-invasive insertions hold significant importance in the field of photoacoustic imaging as they mitigate potential drawbacks related to trauma-induced blood loss and photoacoustic signal attenuation. Additionally, they contribute to maintaining the stability and reproducibility of experimental models. Consequently, our non-invasive approach ensures efficient in vivo imaging while facilitating continuous tracking of small animal models. This approach offers a practical solution to overcome challenges associated with uterine injury and enhances the feasibility of photoacoustic imaging in small animal research. Another widely recognized challenge in vivo imaging involves the influence of physiological motion in animals. Specifically, in this experiment, these factors may result in discontinuities and misalignment within the microvascular network. Nevertheless, by adjusting the anesthetic dosage, rats are induced to maintain minimal breathing while their heart rates are slowed, thus mitigating motion impact on imaging. On the other hand, if the motion artifact occurs, there might be a localized vessel network displacement rather than density change. It's noteworthy that our quantification represents an overall assessment of microvessel density composition distribution, which will not be affected by the density displacement in any direction.

Usually, the maximum amplitude projection (MAP) or depth encoded MAP method is frequently employed for presenting the 3D photoacoustic imaging results in a 2D way [23]. Nonetheless, this approach only preserves the amplitude data of the single maximum value on each A-line, thereby rendering other signals unobservable. Nevertheless, within the endometrium—an area characterized by a dense vascular network, MAP representation may lead to the loss of numerous vascular signals and even result in discontinuity within the microvessel network, as shown in Supplementary Fig. 6. Consequently, we choose to employ the photoacoustic DAP way, which utilizes a transparency display method on each A-line. This technique has the capability to conserve numerous signals at varying depths along each A-line. Compared with MAP, DAP excels in retaining subtle signal details, leading to a notably enriched and coherent vascular network in the processed data. Upon quantifying the MAP and DAP from several datasets, as shown in the Supplementary Fig. 7 (extracted from Supplementary Fig. 6), the differences in density quantification between them all through these datasets can be observed. Although the difference in density extracted from MAP and DAP is always exhibited in each dataset, the density distribution patterns exhibit a high level of consistency.

A higher MVD value observed in endometrial tissue signifies a greater abundance of capillaries [24], thereby indicating good ER [25,26]. Consequently, this article utilizes MVD as a quantitative measure to evaluate ER. Microvessel usually refers to the network of small blood vessels with less than 100 μm [27]. Through immunostaining of endothelial marker CD31, it makes the visualization of the microvessels precise and clear [28], but this method only images microvessels in the top surface layer. MicroCT can capture the 3D morphology of microvessels and the overall distribution of the microvessel network, it provides an overall basket-like distribution of endometrial vascular networks [29]. Similarly, photoacoustic can also obtain the same 3D features as depicted in Fig. 2. Significantly, the PAE imaging technique reveals a greater extent of the vascular network structure, including numerous microvessels that are not detectable in microCT imaging. This disparity can be attributed to the limitations of microCT, which relies on the perfusion of contrast agents that face challenges in accessing all capillaries [30], while photoacoustic imaging achieves these valuable signals from endogenous blood cells [31]. This provides clinical convenience and improves an intuitive understanding of endometrial blood supply, thereby facilitating the evaluation of ER for clinicians in a more efficient and dependable manner.

In this study, we conducted the modeling operation to induce various degrees of endometrial injury, by introducing a electric heating catheter into the uterine cavity through the vagina and adjusting its temperature accordingly. Corresponding to the different physiological conditions from modeling results, the imaging results distinctly reveal the disparities in the distribution of endometrial microvessels between the damaged and normal areas. Consistent with the imaging results, the density-pullback distance curves in Fig. 4 showcased a notable disparity between the density of the normal area and the modeling area becomes evident. The contrast between the mildly damaged area and the severely damaged area lacks sufficient clarity. Thus, the density distribution characteristic was analyzed and displayed in histograms in Fig. 5, it not only demarcates the modeling group (bimodal) from the normal group (single-peak) through distinct peak pattern features but also effectively discerns between mild and severe damage by the density distribution value at the respective damaged peaks. Clearly, the histogram highlights a discernible difference between mild and severe damage after three days of modeling, as evidenced by the distinctive peak structures. This underscores the histogram's capability to accurately distinguish degrees of damage. It's important to note that the density extracted from both photoacoustic slice and DAP images exhibit similar changing trends, but the discriminatory capacity of the photoacoustic slice density is notably deficient. Given that the DAP image provides insight into the overall 3D distribution of microvessels, whereas the slice image solely captures the microvessels from a specific endometrial layer, it's reasonable to believe that photoacoustic DAP gives more precise density distribution results.

As depicted in Supplementary Fig. 8, the HE staining and Masson staining of the endometrium provide compelling evidence that modeling at various temperatures induces distinct degrees of endometrial damage, resulting in impairment of the endometrial vascular system. Diverse extents of such injury correspond to distinct prognosis. Typically, mild injuries can swiftly recover without compromising fertility [32]. However, severe injuries might induce intrauterine adhesions due to the extensive damage, posing challenges in reinstating physiological function and potentially giving rise to secondary infertility [33]. The findings from the rat pregnancy experiment provide valuable insights. Notably, the mild injury group exhibited a substantial recovery, evidenced by the close proximity of embryo numbers to those of normal rats, both on the modeled and unmodeled sides, without any significant disparities. In contrast, the severe injury group painted a strikingly different picture, with just one embryo detected on the modeling side across the three rats. This lone embryo underscores severe endometrial dysfunction, with minimal prospects for recuperation. These results harmonize effectively with the preceding quantitative analysis of endometrial MVD. In the mild injury group's modeled area, there was a

significant recuperation in MVD by the third day. Conversely, the severe injury group displayed a considerably more gradual recovery. This underscores the viability of endometrial MVD as an effective indicator for assessing ER. While the study's sample size might not be exhaustive enough to provide precise density thresholds or ranges, the distinction between normal and abnormal MVD is evidently valuable.

Based on the existing findings, we envision future work in three broad areas. First, to enhance the precision of ER assessment, beyond depicting the microvessel condition within the endometrium, it may be advantageous to visualize the vasculature across distinct uterine layers and concomitantly examine them alongside microvessels. This approach facilitates a comprehensive appraisal of uterine blood supply. This pursuit, however, introduces a new imaging challenge, expanding the depth range of the PAE system and maintaining its resolution. Second, constrained by the repetition rate of the current laser, the present imaging speed remains somewhat sluggish. While imaging of small animals is achievable, the task becomes more demanding for larger animals or potential clinical translation due to the increased A-lines numbers in each B-scan, inevitably leading to a further reduction in frames per second. Consequently, it becomes imperative to contemplate the adoption of lasers with higher repetition frequencies in upcoming endeavors. Lastly, to gain further insights into the recovery and prognosis of varying degrees of endometrial injury in future follow-up studies, treatment interventions will be necessary to facilitate the observation of this process.

5. Conclusion

In this study, for the first time, photoacoustic endoscopy was applied to achieve in vivo imaging in the uterine cavity of small animals. This endeavor resulted in the non-invasive acquisition of a high-resolution, comprehensive, 3D vascular network of endometrial microvessels. Through continuous observation of microvessel changes in the endometrium following varying degrees of injury, we confirmed the effectiveness of PAE in assessing endometrial function by noninvasively monitoring and quantifying MVD changes and thereby predicting ER. It can be hoped that forthcoming endeavors will delve deeper into researching the occurrence and development mechanisms of endometrial injury through the utilization of intrauterine PAE images.

CRediT authorship contribution statement

Shu Chengyou: Methodology. **Lin Riqiang:** Investigation, Funding acquisition. **Zhang Jinke:** Funding acquisition, Data curation. **Xia Qingrong:** Writing – original draft, Validation, Methodology. **Chen Zhiyi:** Supervision, Investigation, Funding acquisition. **Gong Xiaojing:** Writing – review & editing, Supervision, Investigation, Funding acquisition, Conceptualization. **Wang Xiatian:** Methodology. **Xie Zhihua:** Investigation, Funding acquisition. **Lv Shengmiao:** Methodology, Data curation. **Xu Haoxing:** Data curation.

Declaration of Competing Interest

The authors declare that they have no known competing financial interests or personal relationships that could have appeared to influence the work reported in this paper.

Data Availability

Data will be made available on request.

Acknowledgements

This work was supported by the National Natural Science Foundation of China (82027803); Shenzhen Science and Technology Innovation Committee under Grant (JCYJ20210324101612034, JCYJ20220818101417039); Key Laboratory of Biomedical Imaging Science and System, Chinese Academy of Sciences; Guangdong Provincial Key Laboratory of Biomedical Optical Imaging (2020B121201010); Shenzhen Key Laboratory for Molecular Imaging (ZDSY20130401165820357).

Appendix A. Supporting information

Supplementary data associated with this article can be found in the online version at doi:10.1016/j.pacs.2024.100589.

References

[1] D. Pan, J. Yang, N. Zhang, L. Wang, N. Li, J. Shi, H. Zhou, Gonadotropin-releasing hormone agonist downregulation combined with hormone replacement therapy improves the reproductive outcome in frozen–thawed embryo transfer cycles for patients of advanced reproductive age with idiopathic recurrent implantation failure, Reprod. Biol. Endocrinol. 20 (2022) 26, https://doi.org/10.1186/s12958-022-00897-3.

[2] B.A. Lessey, S.L. Young, What exactly is endometrial receptivity? Fertil. Steril. 111 (2019) 611–617, https://doi.org/10.1016/j.fertnstert.2019.02.009.

[3] Y. Zhong, F. Zeng, W. Liu, J. Ma, Y. Guan, Y. Song, Acupuncture in improving endometrial receptivity: a systematic review and meta-analysis, BMC Complement Alter. Med. 19 (2019) 61, https://doi.org/10.1186/s12906-019-2472-1.

[4] T. Karaca, Y. Hulya Uz, R. Karabacak, I. Karaboga, S. Demirtas, A. Cagatay Cicek, Effects of hyperthyroidism on expression of vascular endothelial growth factor (VEGF) and apoptosis in fetal adrenal glands, Eur. J. Histochem. 59 (2015), https://doi.org/10.4081/ejh.2015.2560.

[5] M.P. Karizbodagh, B. Rashidi, A. Sahebkar, A. Masoudifar, H. Mirzaei, Implantation window and angiogenesis, J. Cell. Biochem. 118 (2017) 4141–4151, https://doi.org/10.1002/jcb.26088.

[6] X. Shui, C. Yu, J. Li, Y. Jiao, Development and validation of a pregnancy prediction model based on ultrasonographic features related to endometrial receptivity, (n. d.).

[7] E. Cicinelli, R. Tinelli, A. Lepera, V. Pinto, M. Fucci, L. Resta, Correspondence between hysteroscopic and histologic findings in women with chronic endometritis, Acta Obstet. Gynecol. Scand. 89 (2010) 1061–1065, https://doi.org/10.3109/00016349.2010.498496.

[8] K. Banno, Narrow band imaging hysteroscopy: a comparative study using randomized video images, Int. J. Oncol. (2011), https://doi.org/10.3892/ijo.2011.1131.

[9] R. Tong, Y. Zhou, Q. He, Y. Zhuang, W. Zhou, F. Xia, Analysis of the guidance value of 3D ultrasound in evaluating endometrial receptivity for frozen-thawed embryo transfer in patients with repeated implantation failure, 944–944, Ann. Transl. Med. 8 (2020), https://doi.org/10.21037/atm-20-5463.

[10] Z. Hosseinaee, M. Le, K. Bell, P.H. Reza, Towards non-contact photoacoustic imaging [review], Photoacoustics 20 (2020) 100207, https://doi.org/10.1016/j.pacs.2020.100207.

[11] S. Nitkunanantharajah, K. Haedicke, T.B. Moore, J.B. Manning, G. Dinsdale, M. Berks, C. Taylor, M.R. Dickinson, D. Jüstel, V. Ntziachristos, A.L. Herrick, A. K. Murray, Three-dimensional optoacoustic imaging of nailfold capillaries in systemic sclerosis and its potential for disease differentiation using deep learning, Sci. Rep. 10 (2020) 16444, https://doi.org/10.1038/s41598-020-73319-2.

[12] Y. Qu, P. Hu, J. Shi, K. Maslov, P. Zhao, C. Li, J. Ma, A. Garcia-Uribe, K. Meyers, E. Diveley, S. Pizzella, L. Muench, N. Punyamurthy, N. Goldstein, O. Onwumere, M. Alisio, K. Meyenburg, J. Maynard, K. Helm, E. Altieri, J. Slaughter, S. Barber, T. Burger, C. Kramer, J. Chubiz, M. Anderson, R. McCarthy, S.K. England, G. A. Macones, M.J. Stout, M. Tuuli, L.V. Wang, In vivo characterization of connective tissue remodeling using infrared photoacoustic spectra, J. Biomed. Opt. 23 (2018).

[13] M. Kim, K.W. Lee, K. Kim, O. Gulenko, C. Lee, B. Keum, H.J. Chun, H.S. Choi, C. U. Kim, J.-M. Yang, Intra-instrument channel workable, optical-resolution photoacoustic and ultrasonic mini-probe system for gastrointestinal endoscopy, Photoacoustics 26 (2022) 100346, https://doi.org/10.1016/j.pacs.2022.100346.

[14] C. Miranda, J. Barkley, B.S. Smith, Intrauterine photoacoustic and ultrasound imaging probe, J. Biomed. Opt. 23 (2018) 1, https://doi.org/10.1117/1.JBO.23.4.046008.

[15] Y. Li, R. Lin, C. Liu, J. Chen, H. Liu, R. Zheng, X. Gong, L. Song, *In vivo* photoacoustic/ultrasonic dual-modality endoscopy with a miniaturized full field-of-view catheter, J. Biophotonics. 11 (2018) e201800034, https://doi.org/10.1002/jbio.201800034.

[16] L.V. Wang, S. Hu, Photoacoustic tomography: in vivo imaging from organelles to organs, Science 335 (2012) 1458–1462, https://doi.org/10.1126/science.1216210.

[17] X. Xu, L. Cao, Z. Wang, Z. Xu, B. Zhang, S. Wu, S. Qi, L. Yan, Z. Chen, Creation of a rabbit model for intrauterine adhesions using electrothermal injury, J. Zhejiang Univ. Sci. B 19 (2018) 383–389, https://doi.org/10.1631/jzus.B1700086.

[18] K. Takemori, H. Kanzaki, M. Koshida, I. Konishi, Scanning electron microscopy study on corrosion cast of rat uterine vasculature during the first half of pregnancy, (n.d.).

[19] Z. Li, X. Wang, Y. Guan, X. Yu, J. Liu, Z. Zhang, Uterine artery blood flow and microvessel density by vaginal color Doppler ultrasonography in embryo

implantation failure, Exp. Ther. Med. (2017), https://doi.org/10.3892/etm.2017.5114.
[20] J.-H. Yang, M.-Y. Wu, C.-D. Chen, M.-C. Jiang, H.-N. Ho, Y.-S. Yang, Association of endometrial blood flow as determined by a modified colour Doppler technique with subsequent outcome of in-vitro fertilization, Hum. Reprod. 14 (1999) 1606–1610, https://doi.org/10.1093/humrep/14.6.1606.
[21] J.M. Yang, C. Favazza, J. Yao, R. Chen, Q. Zhou, K.K. Shung, L.V. Wang, Three-dimensional photoacoustic endoscopic imaging of the rabbit esophagus, PLoS One 10 (2015) e0120269, https://doi.org/10.1371/journal.pone.0120269.
[22] J. Zhang, M. Du, Ji Fang, S. Lv, W. Lou, Z. Xie, Z. Chen, X. Gong, In vivo evaluation of endometrium through dual-modality intrauterine endoscopy, Biomed. Opt. Express 13 (2022) 2554, https://doi.org/10.1364/BOE.453191.
[23] H. Estrada, J. Rebling, U. Hofmann, D. Razansky, Discerning calvarian microvascular networks by combined optoacoustic ultrasound microscopy, Photoacoustics 19 (2020) 100178, https://doi.org/10.1016/j.pacs.2020.100178.
[24] Q. Zhao, R. Lin, C. Liu, J. Zhao, G. Si, L. Song, J. Meng, Quantitative analysis on in vivo tumor-microvascular images from optical-resolution photoacoustic microscopy, J. Biophoton. 12 (2019) e201800421, https://doi.org/10.1002/jbio.201800421.
[25] M. Oliveira-Ribeiro, C.A. Petta, L.A.L. De Angelo Andrade, M.M. Hidalgo, A. Pellogia, L. Bahamondes, Endometrial histology, microvascular density and caliber, and matrix metalloproteinase-3 in users of the Nestorone®-releasing contraceptive implant with and without endometrial breakthrough bleeding, Contraception 73 (2006) 634–640, https://doi.org/10.1016/j.contraception.2005.10.013.
[26] S.K. Smith, Regulation of angiogenesis in the endometrium, Trends Endocrinol. Metab. 12 (2001) 147–151, https://doi.org/10.1016/S1043-2760(01)00379-4.
[27] Y. Zhao, D. Ji, Y. Li, X. Zhao, W. Lv, X. Xin, S. Han, C. Hu, Three-dimensional visualization of microvasculature from few-projection data using a novel CT reconstruction algorithm for propagation-based X-ray phase-contrast imaging, Biomed. Opt. Express 11 (2020) 364, https://doi.org/10.1364/BOE.380084.
[28] W. Cai, Y. Li, Q. Yi, F. Xie, B. Du, L. Feng, L. Qiu, Total saponins from Albizia julibrissin inhibit vascular endothelial growth factor-mediated angiogenesis in vitro and in vivo, Mol. Med. Rep. 11 (2015) 3405–3413, https://doi.org/10.3892/mmr.2015.3228.
[29] A. Ogura, T. Nishida, The uterine vascular system of the golden hamster and its changes during the oestrous cycle, J. Anat. 158 (1988) 43–55.
[30] A. Woloszyk, P. Wolint, A.S. Becker, A. Boss, W. Fath, Y. Tian, S.P. Hoerstrup, J. Buschmann, M.Y. Emmert, Novel multimodal MRI and MicroCT imaging approach to quantify angiogenesis and 3D vascular architecture of biomaterials, Sci. Rep. 9 (2019) 19474, https://doi.org/10.1038/s41598-019-55411-4.
[31] M. Heijblom, D. Piras, M. Brinkhuis, J.C.G. Van Hespen, F.M. Van Den Engh, M. Van Der Schaaf, J.M. Klaase, T.G. Van Leeuwen, W. Steenbergen, S. Manohar, Photoacoustic image patterns of breast carcinoma and comparisons with Magnetic Resonance Imaging and vascular stained histopathology, Sci. Rep. 5 (2015) 11778, https://doi.org/10.1038/srep11778.
[32] R. Li, G. Hao, Local injury to the endometrium: its effect on implantation, Curr. Opin. Obstet. Gynecol. 21 (2009) 236–239, https://doi.org/10.1097/GCO.0b013e32832a0654.
[33] T. Kakinuma, K. Kakinuma, Y. Matsuda, M. Ohwada, K. Yanagida, Successful live birth following hysteroscopic adhesiolysis under laparoscopic observation for Asherman's syndrome: a case report, World J. Clin. Cases 10 (2022) 11949–11954, https://doi.org/10.12998/wjcc.v10.i32.11949.

Qingrong Xia, a sonographer at the Affiliated Nanhua Hospital, concurrently pursued a Ph.D. at the University of South China. Her research focuses on the application of endoscopic multimodal photoacoustic imaging within the realm of the gynecological reproductive system

Shengmiao Lv is currently pursing his Master's degree in ShenZhen Institutes of Advanced Technology, Chinese Academy of Science. His research interests include photoacoustic endoscopy imaging and FPGA-based digital signal processing system

Haoxing Xu is currently pursing his Master's degree in ShenZhen Institutes of Advanced Technology, Chinese Academy of Science. His research interests include optical coherence elastography and optical coherence tomography endoscopic imaging

Xiatian Wang is a Ph.D. candidate at the Beijing Institute of Technology. He obtained his Master's and Bachelor's degrees from the Beijing Institute of Technology in 2017 and 2013, respectively. Presently, he serves as a visiting student at the Shenzhen Institute of Technology, Chinese Academy of Science. His research is primarily centered around nonlinear photoacoustic imaging, exploring innovative applications in this field

Zhihua Xie is an Associate Professor at SIAT, CAS. She received her Ph.D. degree from the University of Frache-Comte, France, 2016. She joined SIAT in October, 2016. Dr. Xie's research focuses on the development and applications of photoacoustic endoscopies.

Riqiang Lin received his M.Sc. and B.S. degree from Shenzhen University. He is currently pursuing his Doctoral degree at The Hong Kong Polytechnic University and focuses on the research of photoacoustic endoscopy imaging and ultrasound transducer technology. His current research interests focus on developing novel photoacoustic endoscopic catheters for clinical translation

Jinke Zhang, Ph.D., Assistant Researcher. Shenzhen Institutes of Advanced Technology, Chinese Academy of Sciences, Research Center for Biomedical Optics and Molecular Imaging. He obtained his Ph.D. degree in Engineering from the University of Liverpool in 2018. Currently, he is primarily engaged in the application of photoacoustic/OCT multimodal endoscopic imaging in biomedicine clinical settings.

Chengyou Shu is currently employed at the Shenzhen Institute of Advanced Technology, Chinese Academy of Sciences. He graduated from Nanjing University of Aeronautics and Astronautics with a master's degree in aerospace engineering in 2016. He primarily specializes in embedded software and hardware development for optical and acoustic medical imaging equipment. He has participated in projects supported by the National Key Research and Development Program of China and has published three academic papers.

Zhiyi Chen is the Director of the Institute of Medical Imaging of the University of South China and the Institute of Medical Imaging of Changsha Central Hospital affiliated to the University of South China. His mainly research interested filed is the development and application of novel imaging technology, especially the field of optic/acoustic based multimodal imaging equipment and image fusion technology.

Xiaojing Gong is a professor at Shenzhen Institutes of Advanced Technology, Chinese Academy of Sciences. He received B.S. degree in Mechatronics from the Southeast University in 2000, and Ph.D. degree in Fine Instruments and Mechanics from the University of Science and Technology of China in 2007. His interest focuses on multi-modality endoscopic imaging development and research (including photoacoustic imaging, optical coherent tomography, and ultrasonic imaging) and its clinical translation, such as intravascular imaging, gastrointestinal endoscopy, and reproductive tract endoscopy.